Monthly Notices
of the
ROYAL ASTRONOMICAL SOCIETY

MNRAS **481,** 5236–5246 (2018)
Advance Access publication 2018 September 26

doi:10.1093/mnras/sty2622

Faint γ-ray sources at low redshift: the radio galaxy IC 1531

T. Bassi,[1,2,3]★ G. Migliori,[4,5,6] P. Grandi,[7] C. Vignali,[4,7] M. A. Pérez-Torres,[8] R. D. Baldi,[9] E. Torresi,[4,7] A. Siemiginowska[10] and C. Stanghellini[5]

[1]*INAF – Istituto di Astrofisica Spaziale e Fisica Cosmica di Palermo, Via Ugo La Malfa 153, I-90146 Palermo, Italy*
[2]*Dipartimento di Fisica e Chimica, Universitá degli Studi di Palermo, Via Archirafi 36 – I-90123 Palermo, Italy*
[3]*IRAP, Université de Toulouse, CNRS, UPS, CNES, Toulouse, France*
[4]*Dipartimento di Fisica e Astronomia, Alma Mater Studiorum, Università degli Studi di Bologna, Via Gobetti 93/2, I-40129 Bologna, Italy*
[5]*INAF Istituto di Radioastronomia, Via Gobetti 101, I-40129 Bologna, Italy*
[6]*Laboratoire AIM (CEA/IRFU – CNRS/INSU – Université Paris Diderot), CEA DSM/SAp, F-91191 Gif-sur-Yvette, France*
[7]*INAF – Osservatorio di Astrofisica e Scienza dello Spazio di Bologna, Via Gobetti 93/3, I-40129 Bologna, Italy*
[8]*Instituto de Astrofísica de Andalucía (IAA-CSIC), E-18008 Granada, Spain*
[9]*School of Physics and Astronomy, University of Southampton, Southampton SO17 1BJ, UK*
[10]*Harvard Smithsonian Center for Astrophysics, 60 Garden St, Cambridge, MA 02138, USA*

Accepted 2018 September 19. Received 2018 September 17; in original form 2018 June 3

ABSTRACT

We present a multiwavelength study of IC 1531 (z = 0.02564), an extragalactic radio source associated with the γ-ray object 3FGL J0009.9 − 3206 and classified as a blazar of uncertain type in the Third *Fermi*-Large Area Telescope AGN catalog (3LAC). A core-jet structure, visible in radio and X-rays, is enclosed within a ∼220 kpc wide radio structure. The morphology and spectral characteristics of the kiloparsec jet in radio and X-rays are typical of Fanaroff–Riley type I galaxies. The analysis of the radio data and optical spectrum and different diagnostic methods based on the optical, infrared, and γ-ray luminosities also support a classification as a low-power RG seen at moderate angles ($\theta = 10^\circ$–20°). In the framework of leptonic models, the high-energy peak of the non-thermal nuclear spectral energy distribution can be explained in terms of synchrotron-self-Compton emission from a jet seen at $\theta \sim 15^\circ$. Similarly to other misaligned AGNs detected by *Fermi*, the required bulk motion is lower ($\Gamma_{\rm bulk} = 4$) than the values inferred in BL Lac objects, confirming that, because of the de-boosting of emission from the highly relativistic blazar region, these nearby systems are valuable targets to probe the existence of multiple sites of production of the most energetic emission in the jets.

Key words: galaxies: active – galaxies: individual: IC 1531 – galaxies: jets – gamma-rays: galaxies – radio continuum: galaxies.

1 INTRODUCTION

A decade of observations of the Large Area Telescope (LAT) on board the *Fermi* satellite has significantly expanded our knowledge of the γ-ray sky. Even though the extra-galactic γ-ray sky remains firmly dominated by blazars (Fermi-LAT Collaboration 2015), i.e. active galactic nuclei (AGN) with a jet pointing towards the observer, we have for the first time the possibility to probe the population of faint γ-ray sources. This is comprised of luminous sources at high redshift or intrinsically faint sources at low redshift. The former are important to understand the cosmological evolution of γ-ray blazars (Ajello et al. 2012, 2014, and references therein), hence to trace the growth of the supermassive black holes powering the extragalactic jets (Volonteri et al. 2011; Ghisellini 2013a; Ackermann et al. 2017). The latter includes low-luminosity blazars (Massaro et al. 2017) and a heterogeneous ensemble of sources.

Non-blazar faint γ-ray sources are misaligned AGNs (MAGNs, Abdo et al. 2010b) and star-forming galaxies (Ackermann et al. 2012). In addition, there are a large number of unidentified sources, which hold potential for the discovery of new classes of γ-ray emitters (see e.g. the class of narrow-line Seyfert galaxies, the class of FR 0s; Baldi, Capetti & Giovannini 2015), Tol 1326 − 379, PKS 1718 − 649 (Foschini et al. 2011; Migliori et al. 2014, 2016; D'Ammando et al. 2016; Grandi, Capetti & Baldi 2016; Tavecchio et al. 2018). The LAT MAGNs, i.e. AGNs with a jet that is seen at moderate/large angles, collect radio galaxies (RGs) and steep-spectrum radio quasars (SSRQs). According to the unified model of AGN, MAGNs are the misaligned counterparts of blazars. In blazars, the detection of the high-energy emission is favoured by relativistic effects, which boost and blue-shift the emission from a compact region (so-called blazar region) of the jet moving at high

★ E-mail: bassi@ifc.inaf.it

Lorentz factors ($\Gamma \sim 10$–20, Celotti & Ghisellini 2008). Since the emission from the blazar region is de-boosted and red-shifted at increasing viewing angles, the detection of MAGNs in the GeV band may be indicative of a different emission site or emission mechanism. An example is the RG Centaurus A, where the extended γ-ray component is most likely associated with the radio lobes (Abdo et al. 2010a; Sun et al. 2016).

Modelling of the spectral energy distributions (SEDs) of the LAT MAGNs with one-zone leptonic models implies relatively slow jets with respect to blazars (Chiaberge et al. 2000). Models of stratified jets, where the emission from the fast spine is visible at small viewing angles and that from the slow-moving layer emerges at larger angles, have been considered as a viable alternative (Georganopoulos & Kazanas 2003; Ghisellini, Tavecchio & Chiaberge 2005).

In order to test the different scenarios, we need to target the population of faint γ-ray sources at low redshift. In particular, sources that mark the transition between MAGN and blazars may help to establish whether there is a continuity between the two populations, with the inclination angle as the main parameter driving the change in the SED. Understanding the link between orientation and γ-ray emission is also important to constrain the contribution of MAGNs to the extragalactic γ-ray background (EGB). In fact, according to recent studies (Inoue 2011; Di Mauro et al. 2014; Fornasa & Sánchez-Conde 2015), RGs and star-forming galaxies could account for a significant fraction of the EGB.

In this paper, we present a multiwavelength study of the radio source IC 1531 ($z = 0.02564$), which is associated with the LAT source 3FGL J0009.9 − 3206. In the third catalog of AGN detected by *Fermi*-LAT (3LAC, Ackermann et al. 2015), it is classified as a blazar of uncertain type. The main goals of our study are to assess the classification of IC 1531 and to investigate the nature of its high-energy emission. Throughout this paper, the following cosmological parameters are assumed: $H_0 = 67.8\,\mathrm{km\ s^{-1}\ Mpc^{-1}}$, $\Omega_m = 0.3$, and $\Omega_\lambda = 0.7$ (Planck Collaboration XIII 2016). At the source distance, 1 arcsec corresponds to 514 pc.

2 IC 1531

IC 1531 (also known with the name PKS 0007-325) is an early-type lenticular galaxy (Loveday 1996) located in a low-density environment (O'Sullivan, Sanderson & Ponman 2007). It is present in several surveys and catalogues, but it has not been extensively studied.

The radio map at 1.4 GHz of the *National Radio Astronomy Observatory (NRAO) Very Large Array Sky Survey* (NVSS, Condon et al. 1998) shows an asymmetric jetted radio source (see Fig. 1), which is powered by the active nucleus. The south-eastern radio lobe has a ∼220 kpc projected extension. The total flux density at 1.4 GHz is 350 mJy (Ekers et al. 1989). In Section 3, we analysed the archival radio observations and obtained the flux densities of the radio components at 1.4–1.5 and 8.4 GHz (see Table A1).

The measured flux densities near 1 mm lie close to the extrapolation of the core data at radio frequencies, supporting a non-thermal origin of the millimetre flux, while the emission of the host galaxy clearly emerges in the infrared-optical band (Knapp & Patten 1991). The weak excess that is visible at 100 μm is most likely of thermal origin and due to radiation from cool dust (Knapp, Bies & van Gorkom 1990) heated by massive stars (Kennicutt 1998).

Based on the optical spectrum reported in the *6 degree field galaxy survey* (6dFGS; Jones et al. 2004, 2009), IC 1531 was classified as an AGN with weak lines in absorption and emission (Mahony et al. 2011).

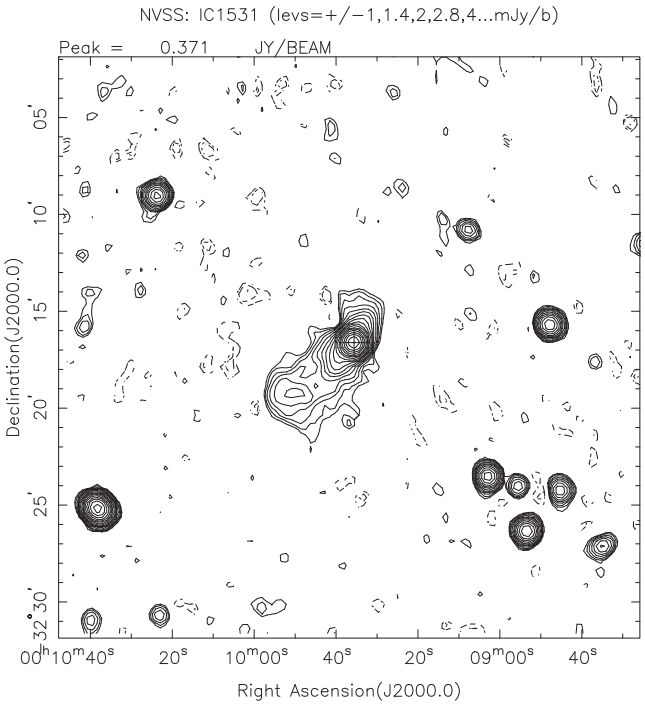

Figure 1. NVSS contour map of IC 1531 at 1.4 GHz. The radio structure in the centre of the image is ∼220 kpc extended.

O'Sullivan et al. (2007) studied the galaxy and its environment in X-rays using observations by the *XMM–Newton* mission and the *Chandra X-ray observatory*. The central AGN dominates the X-ray output ($F_{[0.4\text{–}7]\,\mathrm{keV}} \sim 4.2 \times 10^{-13}$ erg cm^{-2} s^{-1}), together with an extended ($\lesssim$7.5 arcsec) component oriented in the direction of the radio jet (O'Sullivan et al. 2007). The source is surrounded by a relatively cold (∼0.55 keV) and compact X-ray halo (O'Sullivan et al. 2007). The authors concluded that the AGN could have induced gas-mass-loss either via AGN-driven winds or via jet stripping.

In γ-rays, IC 1531 is associated with 3FGL J0009.9-3206, a source reported in the *third Fermi-LAT source catalog* (3FGL, Fermi-LAT Collaboration 2015). 3FGL J0009.9-3206 is detected at the 5.5σ significance level with a flux in the 1–100 GeV band of $(2.77 \pm 0.62) \times 10^{-10}$ ph cm^{-2} s^{-1} and a power-law photon index $\Gamma_\gamma = 2.3 \pm 0.1$.

3 RADIO

We downloaded publicly available Karl G. Jansky Very Large Array (VLA) data of IC 1531 taken in A configuration at 1.5 GHz on 1987 Jul 7, at 1.4 GHz on 1995 Jul 24 (project codes AV0151 and AG0454, respectively), and at 8.5 GHz on 1998 May 19 (project code AH0640). We used standard routines within the NRAO *AIPS* package for all data reduction steps, including amplitude and phase calibration, as well as imaging; our results are summarized in Table 1. We show in Fig. 2 the 8.5 GHz image of IC 1531 (contours), where the coincidence of the radio core with the X-ray nuclear emission is evident. The position of the 8.5 GHz peak is RA = $00^{\mathrm{h}}09^{\mathrm{m}}35^{\mathrm{s}}.56057$, Dec. = $-32^\circ16'36''.9000$ (J2000.0).

The 1.4–1.5 GHz flux densities (both peak and total) are compatible with a non-variability of the source in the two epochs, assuming a 10 per cent uncertainty in the amplitude calibration. In fact, the differences in the flux densities of the peaks are enhanced because of the different FWHM sizes. We therefore restored the two images

Table 1. Log of the VLA observations.

Date	Frequency (GHz)	FWHM (arcsec^2)	rms (mJy beam^{-1})	σ (mJy beam^{-1})	Peak flux density (mJy beam^{-1})	Total flux density (mJy)
1987-Jul-07	1.47	3.6 × 1.3	0.7	24	239	340
1995-Jul-24	1.38	2.4 × 1.2	0.2	20	203	332
1998-May-19	8.46	0.6 × 0.2	0.1	15	296	404

Note. The FWHM corresponds to the natural synthesized beam obtained at each epoch. The quoted 1σ values are the result of adding in quadrature the quoted rms value for each map and the calibration uncertainty, assumed to be of 10 per cent at 1.4–1.5 GHz and 5 percent at 8.5 GHz.

Table 2. Log of the X-ray observations.

Telescope/Instrument	ObsID	Date	Exp. time	Net count rate
XMM–Newton/pn	0202190301	2004-May-20	12.5	2.8×10^{-1}
XMM–Newton/MOS1	0202190301	2004-May-20	20.5	7.3×10^{-2}
XMM–Newton/MOS2	0202190301	2004-May-20	20.5	7.7×10^{-2}
Chandra/ACIS-S	5783	2005-Aug-21	39.5	1.1×10^{-1}
Swift/XRT	0046394001	2011-Nov-12	1.0	1.2×10^{-2}
Swift/XRT	0046394002	2012-Apr-22	3.7	1.7×10^{-2}

Note. The exposure times are corrected for bad time intervals (e.g. high flaring). The net count rates refer to the extraction region of the total emission of each instrument (see Section 4) in the 0.5–7 keV energy band.

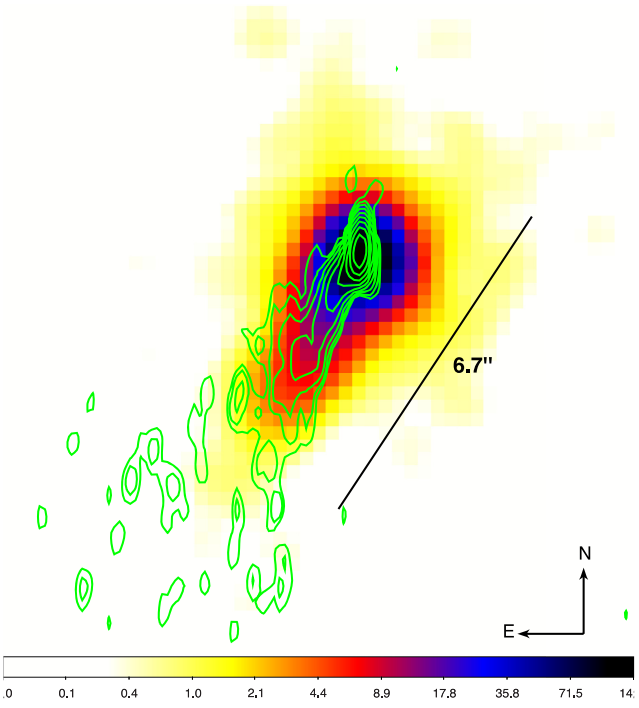

Figure 2. *Chandra* 0.5–7 keV ACIS-S image, at 0.492 arcsec pixel^{-1} resolution, and overlaid VLA 8.5 GHz contours of IC 1531. Contour levels are 4rms$\times\sqrt{2}^n$, with rms = 0.1 mJy beam^{-1}, the natural beam size is 0.6 × 0.2 arcsec^2.

with a common beam. The difference in the resulting peak flux densities was, as expected, smaller than in the case of the natural synthesized beams, confirming that there is neither evidence for nuclear, nor extended variability of the source within 1σ.

4 X-RAY OBSERVATIONS AND ANALYSIS

We retrieved and analysed the publicly available *Chandra*, *XMM–Newton*, and *Swift* observations of IC 1531 (see Table 2).

IC 1531 was observed with the ACIS-S camera on-board the *Chandra X-ray observatory* for ∼40 ks on 2005 August 21 (ObsID 5783). We reprocessed the data using the `chandra_repro` script in the *Chandra Interactive Analysis of Observation (CIAO)* 4.7 software and the *Chandra Calibration Data Base* CALDB v.4.6.9. We excluded high-flaring background periods. The net exposure time after filtering was 39.2 ks. We applied the sub-pixel event-repositioning algorithm (`pix_adj = EDSER`), which optimizes the image resolution.

In Fig. 2, we show the 0.5–7 keV *Chandra* image overlaid the VLA radio contours at 8.4 GHz (see Section 3). The unresolved X-ray core of IC 1531 is clearly visible. Extended (6.7 arcsec) X-ray emission is present in the region coincident with the south-eastern radio jet together with a faint X-ray halo around the point source.

We used `specextract` to obtain the spectra, and the relative response files, of the X-ray emission in the core and the jet regions. For the core, we selected a circular region of 1.4 arcsec radius centred on the unresolved source. The spectrum of the extended jet was extracted from a rectangular box (angular dimensions of 4.2 arcsec × 5.4 arcsec). In addition, for a comparison with the *XMM–Newton* observation, we extracted the spectrum of the total X-ray emission of IC 1531 using an elliptical region (4.1 and 6 arcsec being the angular dimensions of the minor and major axis, respectively). We extracted the background of the core from 5 contiguous circular regions (1.1arcsec radius) that are free from X-ray sources. In order to apply the χ^2 statistics, the data were grouped so that there are at least 15 counts in each spectral bin. Using PIMMS, we estimated a 10 per cent pile-up fraction for the 0.5–7 keV count rate of 7.96 cts s^{-2} in the core region. The background spectrum of the extended jet was extracted from a region at the same distance as the jet (1.4–6.8 arcsec) from the X-ray peak, in order to account

Table 3. Best-fitting model (power law × APEC) of the X-ray spectrum extracted from IC 1531 core region. The Galactic column density is $N_H = 1.69 \times 10^{20}$ cm^{-2} (Kalberla et al. 2005). The errors are quoted at 90 percent level for each parameter (Avni 1976).

kT (keV)	Γ	χ^2_ν(dof)	$F_{[0.5-2]\,PL}$ (erg cm^{-2} s^{-1})	$F_{[0.5-2]\,TE}$ (erg cm^{-2} s^{-1})	$F_{[2-10]\,PL}$ (erg cm^{-2} s^{-1})	$L_{[2-10]\,PL}$ (erg s^{-1})
(1)	(2)	(3)	(4)	(5)	(6)	(7)
$0.6^{+0.2}_{-0.2}$	$2.2^{+0.1}_{-0.1}$	1.16(123)	$2.8^{+0.3}_{-0.3}$	$0.2^{+0.1}_{-0.1}$	$2.5^{+0.3}_{-0.2}$	$3.9^{+0.4}_{-0.4}$

Note. Columns: (1) Plasma temperature (APEC component), (2) photon index, (3) reduced χ^2, (4) unabsorbed 0.5–2 keV flux of the power-law component in unit of 10^{-13} erg cm^{-2} s^{-1}, (5) unabsorbed 0.5–2 keV fluxes of the thermal component in unit of 10^{-13} erg cm^{-2} s^{-1}, (6) unabsorbed 2–10 keV flux of the power-law component in unit of 10^{-13} erg cm^{-2} s^{-1}, and (7) unabsorbed non-thermal 2–10 keV luminosity in units of 10^{41} erg s^{-1}.

for the possible contribution of the diffuse thermal emission and the core's non-thermal emission.[1] The jet and background spectra were simultaneously fit. The background best-fitting model was a steep power law ($\Gamma = 2.9$), and the estimated contribution to the 2–10 keV flux is below 10 per cent.

A ∼24 ks *XMM–Newton* observation of IC 1531 was performed on 2004 May 20. The raw data were processed with the *XMM–Newton* Science Analysis System (SAS v 14). After filtering for background flares, the net exposure times were 12.5 ks for the pn and 20.5 ks for the MOS1 and MOS2. The X-ray emission of the core and jet of IC 1531 are unresolved at the angular resolution of *XMM–Newton* (FWHM ∼6 arcsec). Therefore, we extracted a single 0.5–7 keV spectrum from a circular region of 30 arcsec radius for the pn and 40 arcsec radius for the MOS1 and MOS2 (enclosing ∼90 per cent of the total flux of a point-like source) and verified that the emission is not affected by pile-up effects. The background spectra were obtained from blank-sky regions (30 and 40 arcsec radius, respectively, for pn and MOS) located on the same chip of our source. We grouped the spectra so that each spectral bin has a minimum of 25 counts.

The *X-Ray Telescope* (XRT), on board the *Neil Gehrels Swift Observatory* observed IC 1531 twice in photon-counting mode: the first observation (obsID = 00046394001) was carried out on 2011 November 12 (1.04 ks), while the second pointing (obsID = 00046394002) targeted the source on 2012 April 22 (3.72 ks). The X-ray data were processed and spectra were extracted using the online product generator available at http://www.swift.ac.uk/user_objects/ using default settings (Evans et al. 2009). The number of net (i.e. background subtracted) counts in the 0.3–10 keV band are 12 and 63; fitting the admittedly low counting statistics spectra separately with Cash statistics (Cash 1979) and adopting a power-law model indicated that no significant variability was present between the two observations, so the two data sets were summed. The final spectra were grouped to have at least 1 count per spectral bin, so the data can be fitted with the Cash statistic.

4.1 Spectral analysis results

The *Chandra* spectrum of the core region is best fitted by a composite model with a steep power law ($\Gamma = 2.2 \pm 0.1$) plus a thermal component (an APEC model in XSPEC) with a plasma temperature of 0.6 ± 0.2 keV. The Galactic column density is $N_H = 1.69 \times 10^{20}$ cm^{-2} (Kalberla et al. 2005). The best-fitting parameters are reported in Table 3.

We observed a deviation of the data from the model in the soft (0.5–2 keV) energy band. In principle, the flattening of the spectrum could be due to an intrinsic absorber ($N_{H,int} = 4.50 \times 10^{20}$ cm^{-2}), however, this additional spectral component is not required to model the *XMM–Newton* and *Swift* spectra, suggesting that this is rather an effect of the pile-up.

The fit of the spectrum of the total emission of IC 1531 gave consistent results. Confirming the results of O'Sullivan et al. (2007), the X-ray emission is dominated by the contribution of the AGN: the unabsorbed non-thermal luminosity in the 0.5–10 keV energy band is 8.3×10^{41} erg s^{-1}. The thermal radiation of the gas halo ($L = 7.4 \times 10^{40}$ erg s^{-1}) represents less than 10 per cent of the total X-ray luminosity.

A comparison between the fits of the *Chandra* and *XMM–Newton* spectrum shows a slight difference in the fraction of the soft X-ray flux attributed to each, thermal and non-thermal, component. However, this seems rather due to a combination of effects, i.e. the different sizes of the extraction region and the higher sensitivity of *XMM–Newton* with respect to *Chandra* to low surface brightness. Similarly, although there is an indication of a decrease of the X-ray flux in the *Swift* observations, the limited statistics of the *Swift* spectra leaves the spectral parameters unconstrained and makes difficult to verify it. Thus, we conclude that, if real, a variation of the X-ray flux between 2004/5 and 2012 would be smaller than a factor of 2.

The X-ray emission of the extended jet is continuous and progressively decays with the increasing distance from the core. The best-fitting model of the extended jet spectrum is again a power law with a steep photon index ($\Gamma = 2.2 \pm 0.2$). The unabsorbed non-thermal X-ray flux is $F_{X,\,jet} = (4.2 \pm 0.6) \times 10^{-14}$ erg cm^{-2} s^{-1}, which corresponds to a 2–10 keV luminosity of 6.6×10^{40} erg s^{-1}.

5 OPTICAL PROPERTIES

IC 1531 has been classified as an AGN with weak narrow emission lines (Mahony et al. 2011). In fact, the 6dFGS optical spectrum only shows weak narrow Hα and [O III] and no broad lines, arguing against a classification as a flat spectrum radio quasar (FSRQ). The equivalent widths (EWs) for the Hα and [O III] lines are 1.6 ± 0.4 and 1.7 ± 0.4 Å, respectively. They are lower than 5 Å, which is the typical limit set to identify BL Lac objects (Stickel et al. 1991). However, note that the combination of a low sensitivity and an intrinsically weak line-emitting AGN, diluted by a dominant galaxy

[1] In fact, up to 10 per cent of the point-source flux should be spread at $\gtrsim$1.4 arcsec radius from the peak of the emission (see the Proposer's Observatory Guide, http://cxc.harvard.edu/proposer/POG/).

continuum, such as FR Is (Buttiglione et al. 2009), can equally lead to small EWs.

Since the 6dFGS spectrum is not calibrated, we perform a qualitative photometric flux calibration, similar to the approach used by Grandi et al. (2016) to calibrate the 6dFGS spectrum of Tol 1326 − 379. Such method was already tested on a group of seven early-type emission-line galaxies in common between the 6dFGS and the SDSS surveys. To normalize the spectrum, we use the *J*-band image from the two micron all sky survey (2MASS, Skrutskie et al. 2006). After degrading the *J*-band image to match the seeing of the 6dFGS survey (∼5.7 arcsec), we extract the flux from the image from an aperture of 6.7 arcsec, consistent with the diameter of the 6dFGS fibre where the spectrum comes from, and we measure $J = 12.12 \pm 0.2$. To convert the flux into optical wavelenghts, we adopt a $V{-}J = 2.43$ typical of early-type galaxies (Mannucci et al. 2001). Assuming that the derived *V*-band magnitude is consistent with the spectrum continuum flux in the optical band of our object, we calculate from the EW the emission line fluxes, 1.3×10^{-14} and 8.2×10^{-15} erg s^{-1} cm^{-2}, corresponding to luminosities of 2.2×10^{40} and 1.4×10^{40} erg s^{-1} for Hα and [O III], respectively. The tentative flux calibration of the spectrum yields to an uncertainty of a factor of 4 on the calculated fluxes and luminosities.

We can infer the BH mass, M_{BH}, of the target from its *K*-band magnitude using the empirical relation found by Marconi & Hunt (2003) between the near-infrared bulge luminosity and the M_{BH}. We use the *K*-band 2MASS total magnitude (9.55 ± 0.03) to calculate its luminosity (4.35×10^{11} L$_\odot$). The BH mass estimated within a factor of ∼3 is 1.1×10^9 M$_\odot$.

Taking advantage of the [O III] and M_{BH} measurements, we can also infer other information on the AGN properties of IC 1531. Its bolometric luminosity L_{bol} corresponds to 4.8×10^{43} erg s^{-1} using the relation $L_{bol} = 3500 \times L_{[O\,III]}$ (Heckman et al. 2004) valid for low-luminosity radio AGN with similar luminosity of IC 1531. This value, along with the BH mass, leads to the Eddington luminosity ratio, L_{bol}/L_{Edd}, of 3.5×10^{-4} (within an error of a factor ∼5), indicating a low-luminosity accretion disc, typical of Low Excitation Radio Galaxies (LERG, Best & Heckman 2012).

6 CLASSIFICATION

In the 3LAC (Ackermann et al. 2015), IC 1531 is defined as blazar of uncertain type (BCUI) as the optical spectrum is considered not sensitive enough to discriminate between FSRQ and BL Lac. Our detailed study allows a more accurate classification.

The radio power, $P_{1,4\,GHz} = 5.47 \times 10^{23}$ W Hz^{-1}, and the absolute magnitude in the *R*-band, $M_R = -23.37$, locate IC 1531 in the region mainly occupied by FR I RGs in the radio luminosity versus optical luminosity plane of Ledlow & Owen 1996 . Moreover, its NVSS radio map (Fig. 1) shows a lobe-like south-eastern structure of ∼220 kpc, suggesting a misaligned jet. At a viewing angle of ∼5°, the corresponding de-projected total linear size, assuming source symmetry, would exceed 5 Mpc. Incidentally, we note that low-power RGs similar to IC 1531 do not seem to reach Mpc extension (see Capetti, Massaro & Baldi 2017a,b), that is preferentially observed in powerful radio sources (see 3CR and 2Jy sources; Singal 1993; Ishwara-Chandra & Saikia 1999).

In the colour–colour *WISE* diagram (Wright et al. 2010), its magnitudes ($w1 - w2 = 0.031$ and $w2 - w3 = 1.288$) locate IC 1531 in the elliptical galaxy zone, indicating that the non-thermal emission of the source is not the dominant contribution at wavelengths 3.4–12 μm. The stellar population is also dominant in the optical spectrum (see Section 5), although the [O III]] and Hα lines are detected. In principle, it is difficult to distinguish between a low-luminosity BL Lac object and a misdirected RG in the optical band when the AGN is overwhelmed by the galaxy emission. We then took advantage of the diagnostic plane proposed by Torresi et al. (2018) to investigate this issue. They showed that the ratio between the [O III]] line and the 2–10 keV luminosity ($R_{[O\,III]]}$) is a useful tool to separate misaligned and aligned jets. As the optical emission line is isotropically emitted by circumnuclear gas, while the X-ray photons are emitted by the jet, $R_{[O\,III]]}$ is expected to increase with the jet inclination (i.e. when the Doppler boosting becomes less important and the X-ray luminosity less amplified). The average value measured for FR Is[2] is $< R_{[O\,III]]} >= -1.7 \pm 0.2$ (Torresi et al. 2018), while BL Lacs have generally lower values $< R_{[O\,III]]} >= -3.3 \pm 0.2$ in agreement with the Doppler boosting of the X-ray radiation. The estimated ratio for IC 1531 is $R_{[O\,III]]} = -1.4 \pm 0.9$, similar to FR Is, suggesting that our source shares the same optical X-ray properties of FR I RGs.

Finally, we note that the source is a low-luminosity γ-ray emitter ($\mathrm{Log}\, L_{\gamma>1\,GeV\,[erg\,s^{-1}]} = 42.3 \pm 0.2$) with a steep spectrum ($\Gamma_\gamma = 2.3 \pm 0.1$). In the diagnostic $\Gamma_\gamma - L_{\gamma\,[>1\,GeV]}$ plane (Abdo et al. 2010c), the different class of AGN lie in different parts of the diagram. FSRQs and *steep spectrum radio quasars (SSRQs)* occupy the right-hand side of the plane at higher gamma luminosity and steep spectra, while the BL Lacs are located in the bottom right-hand side of the diagram, having lower luminosity and flatter spectra. The majority of the RGs are arranged at low luminosities outside the blazar strip.[3] IC 1531 falls exactly in the zone populated by RGs (Fig. 3).

On the basis of the multiband properties, we conclude that IC 1531 is an FR I RG showing a moderate Doppler boosted flux amplification.

7 NUCLEAR SED

We assembled the broad-band SED of the core of IC 1531 by combining the analysed data with those available in literature and in online data bases (see Table A1). Although the data are not simultaneous, we note that the multi-epoch observations in the radio and X-ray bands do not indicate significant variability. Similarly, the 3FGL reports a variability index of 42.5, which indicates a low probability for the source to be variable in the γ-ray band. The observed nuclear SED of IC 1531 is shown in Fig. 4. The emission of the host galaxy dominates the SED in the optical-IR band. There is no evidence of a contribution of the disc continuum emission, confirming that the AGN is powered by a low-luminosity radiatively inefficient accretion disc (see also Sec. 5).

[2]The sample is composed by 35 FR Is belonging to the 3CR and 3CRR catalogs. The average value is estimated using the Kaplan–Meyer estimator in ASURV including upper limits (Lavalley, Isobe & Feigelson 1992).

[3]We note that a number of MAGNs are found in the region occupied by blazars (see Fig. 3). Indeed, these targets display a blazar-like, flaring behaviour (see for example PKS 0521-36, D'Ammando et al. 2015), and it is plausible that their small-scale jets are more closely aligned with the observer's line of sight. Similarly, there is not a clear boundary between BL Lacs and FSRQs. One can find transitional sources, which have intermediate properties between high- and low-power radio sources (Sambruna et al. 2007). In addition, it should be noted that an FSRQ caught at the time of a flare can be misclassified as a BL Lac (Ghisellini et al. 2011).

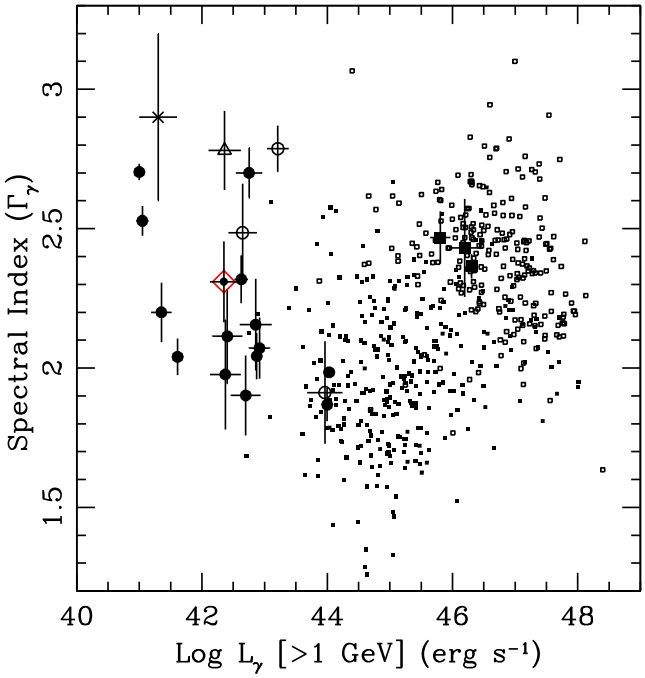

Figure 3. γ-ray spectral slope, Γ_γ, versus 1–100 GeV luminosity. IC 1531 (red diamond) is located in the 3LAC MAGN (FRIs, FRIIs; filled and empty circles, respectively, and SSRQs; big filled squares) region and outside the Blazar (BL LAcs, FSRQs; small filled and empty squares, respectively) zone. The FR0 RG TOL 1326-379 (empty triangle; Grandi et al. 2016) and the compact symmetric object PKS1718-649 (black cross; Migliori et al. 2016) are also shown.

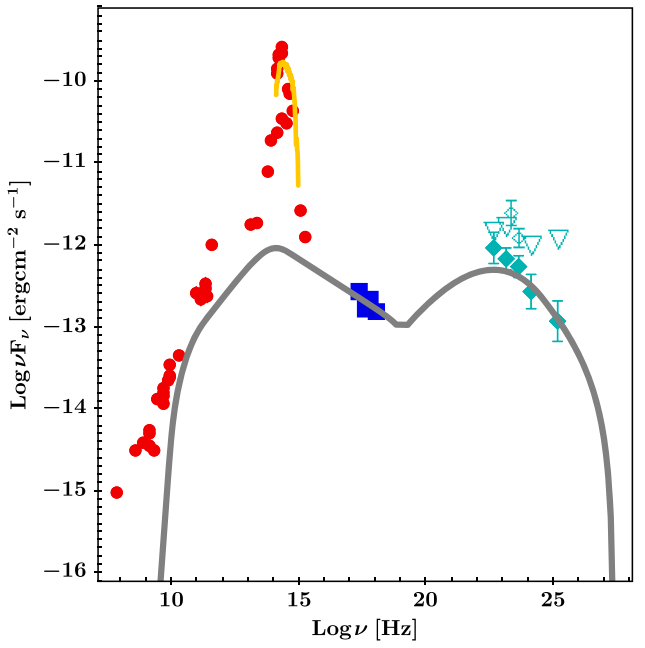

Figure 4. The observed nuclear SED of IC 1531 is described by a leptonic, one-zone synchrotron-SSC model, assuming an observer's viewing angle $\theta = 15°$(grey thick line). The model parameters are reported in Table 4. The filled red points are the data collected from the literature and online archives (see Table A1), the filled diamonds are the γ-ray fluxes from the 3FGL, the empty diamonds are from the 2FGL, and the empty triangles are the upper limits. The filled squares are the *Chandra* fluxes of the core. The orange line is the galaxy template (Mannucci et al. 2001).

The upper limit to the disc's UV luminosity derived from the observations ($L_{\rm UV} \lesssim 3.0 \times 10^{42}$ erg s^{-1}, see Table A1) is significantly smaller than the AGN bolometric luminosity derived in Section 5.

The compact jet produces radio to γ-ray non-thermal emission. We modelled the jet's SED in the framework of leptonic, one-zone models. The emission is produced by a spherical blob of radius $R_{\rm blob}$, moving with a bulk Lorentz factor $\Gamma_{\rm bulk}$. We assumed a conical jet and set $R_{\rm blob} = \psi z_{\rm dist}$, with $z_{\rm dist}$ and ψ being the distance from the base of the jet and the jet's semi-opening angle, respectively, and we fixed $\psi = 0.1$ rad (see e.g. Migliori et al. 2014, for details). Interacting with the jet's magnetic field (B), the electrons in the blob radiate synchrotron photons, which are up-scattered to higher energies (synchrotron self-Compton, SSC; Maraschi, Ghisellini & Celotti 1992). Given the limits on the disc luminosity and emission lines, Comptonization of external photon fields (including disc's reprocessed emission in the broad line regions and torus; Sikora, Begelman & Rees 1994) is not a significant contribution and was not considered in the modelling.

Constraints to some of the model parameters could be derived from the observations (see e.g. Tavecchio, Maraschi & Ghisellini 1998; Ghisellini 2013b). The features of the observed SED can be used to define the shape of the energy distribution of the radiating electrons $N(\gamma)$. The synchrotron spectrum peaks at approximately $\nu_{\rm syn} \sim 10^{13-15}$ Hz and extends to the X-ray band, as the steep X-ray spectral index ($\alpha_X = 1.2 \pm 0.1$) indicates. In the high-energy band, the SSC peak, $\nu_{\rm SSC}$, can be located at $\approx 10^{22-24}$ Hz. The observed SED suggests that the fluxes of the two peaks are similar, $F_{\rm syn/SSC,peak} \lesssim 10^{-12}$ erg cm^{-2} s^{-1}. We set the synchrotron spectral index at energies beyond the peak equal to $\alpha_{\rm syn,2} = \alpha_X$, a value that is also consistent with the spectral index measured by *Fermi*-LAT, and we assumed a slope $\alpha_{\rm syn,\,1} \sim 0.6$ below the peak. Based on these features, we assumed a broken power-law shape for $N(\gamma)$. The energy break $\gamma_{\rm b} = (3\nu_{\rm SSC}/4\nu_{\rm syn})^{1/2}$ falls in the range $\approx 10^{3-4}$ and the spectral indexes below and above $\gamma_{\rm b}$ are $p_1 \equiv 2\alpha_{\rm syn,1} + 1 = 2.2$ and $p_2 \equiv 2\alpha_{\rm syn,\,2} + 1 = 3.4$, respectively.

The radio observations provided us with constraints on the inclination of the jet with respect to the observer's line of sight, θ. A maximum θ of $\sim 30°$ was inferred using the relation between the core radio power at 5 GHz and the total radio power at 408 MHz in Giovannini et al. (2001). Based on the jet–counterjet radio flux ratio and keeping into account the uncertainties on the measurements (see Appendix B for the details), we derived a range of θ between $\sim 10°$ and $\sim 20°$. We assumed $\theta = 15°$ as fiducial value and investigated the implications of smaller/larger values for the jet structure and energetics. The modelled non-thermal beamed SED of the jet for $\theta = 15°$ is shown in Fig. 4. The values of the model parameters are reported in Table 4 together with the jet's Poynting flux (L_B), the kinetic power ($P_{\rm jet} = L_{\rm e} + L_{\rm p}$, with $L_{\rm e}$ and $L_{\rm p}$ powers in radiating electrons and cold protons, respectively) and the radiating power ($L_{\rm rad}$). We note that the inferred jet powers are comparable with the bolometric AGN luminosity derived from [O III] luminosity, confirming that the SED of this object is jet-dominated. Given the small dimensions and the value of the B field of the emitting region, the modelled synchrotron spectrum is self-absorbed at $\lesssim 10^{11}$ Hz and does not account for the radio emission at <GHz frequencies, which is assumed to come from larger regions of the jet. Similarly, at frequencies below the synchrotron peak the modelled jet emission remains below the data points, as the *WISE* data indicate that the host galaxy is still dominant at 10^{13} Hz (see Section 6).

Table 4. Model parameters for the jet nuclear SED of IC 1531. Columns: (1) jet viewing angle in degrees; (2) bulk motion of the emitting region; (3,4,5) minimum, maximum, and break random Lorentz factors of the radiating electrons (a broken power-law shape of the energy distribution is assumed); (6) energy densities of the electrons/magnetic field in the blob comoving frame in units of ergs cm^{-3}; (7) jet Poynting flux; (8) power in bulk motion of the radiating electrons; (9) power in bulk motion of cold protons (one cold proton per radiating electron is assumed); (10) jet kinetic power ($L_e + L_p$); and (11) jet radiative power. Quantities in 7–11 are in logarithmic scale (in units of erg s^{-1}).

θ (1)	Γ_{bulk} (2)	γ_{min} (3)	γ_{max} (4)	γ_b (5)	$U_e^{'}/U_B^{'}$ (6)	L_B (7)	L_e (8)	L_p (9)	P_{jet} (10)	L_{rad} (11)
Radio galaxy										
12	4.5	180	5×10^6	9×10^3	$8.7 \times 10^{-3}/2.5 \times 10^{-5}$	41.23	43.46	43.90	44.04	41.94
15	4	180	5×10^6	9×10^3	$7.0 \times 10^{-3}/1.4 \times 10^{-4}$	41.72	43.11	43.56	43.69	42.15
20	2	180	5×10^6	7.5×10^3	$9.5 \times 10^{-3}/2.6 \times 10^{-4}$	41.49	42.75	43.18	43.33	42.18
Blazar										
5	10	180	5×10^6	8.0×10^3	$5.4 \times 10^{-3}/2.6 \times 10^{-6}$	40.78	43.80	44.25	44.38	41.02

8 DISCUSSION

The multiwavelength study of IC 1531 presented in the previous sections favours a classification of the source as an RG. The radio and X-ray brightness of the large-scale radio structure is decreasing moving out of the core, and the X-ray spectrum of the kpc jet is compatible with being synchrotron emission, as typical for low-power, FR I RGs (Harris & Krawczynski 2006, for a review).

IC 1531 shares the properties of the LAT detected FR Is (see Torresi et al. 2018, and references therein). These sources are continuously detected by LAT and show low level or no variability in γ-rays (Fermi-LAT Collaboration 2015; Sahakyan, Baghmanyan & Zargaryan 2018). The notable exception is NGC 1275 that couples a long-term continuous brightening with short-term (down to few days) flaring activity (Tanada et al. 2018). However, this radio source is peculiar in that its radio activity has recently restarted and shows strong evolution of its small-scale radio structure (Nagai et al. 2010). Differently, FR IIs are detected only when they undergo rapid and intense flares, which appear to be accompanied by the ejection of a new component (Grandi, Torresi & Stanghellini 2012; Casadio et al. 2015; Tanaka et al. 2015). As for IC 1531, the nuclear X-ray emission of LAT FRIs is non-thermal. The X-ray emission of the broad line RGs observed by *Fermi* is instead dominated by accretion-related processes (Grandi & Palumbo 2007; Kataoka et al. 2011). Indeed, FRIIs and some BLRGs, such as 3C 120, have bright disc emission and, likewise FSRQs, there could be a contribution from external Compton on the photons from the disc (or reprocessed in the broad line regions and torus).

In IC 1531, the radio data suggest a θ ranging from $\sim$10° to $\sim$20°. Within these limits, we were able to explain the nuclear SED with a synchrotron and SSC model by assuming a moderate/low bulk motion Γ_{bulk} $\sim$2–4.5. Such values are in agreement with those inferred by modelling the SED of other MAGNs detected by *Fermi*, while BL Lac sources have typically Γ_{bulk} $\sim$10–20.

In the framework of the unified model of jetted AGNs (Urry & Padovani 1995; Padovani et al. 2017), RGs are the misaligned counterparts of blazars and the jets of the two classes should have the same structure. The hypothesis to reconcile the different Γ_{bulk} is that, at increasing viewing angles, the de-boosting of the emission from the blazar region makes visible the radiative components of mildly relativistic regions (Chiaberge et al. 2000). Indeed, the Doppler factors of these slower regions, δ $\sim$2–7, are smaller than in BL Lac objects ($\delta \gtrsim 10$), limiting the factor of amplification of the intrinsic luminosities, $L^{'}$, in the observer reference frame ($L = \delta^4 L^{'}$). Hence, the observed γ-ray fluxes of MAGNs are relatively faint and require sensitive observations to be detected.

The sensitivity reached in 10 years of LAT sky survey opens at the possibility to realize a tomography of the regions of the jet where the most energetic emission is produced. In the case of IC 1531, for simplicity we considered a dynamical structure that is orthogonal to the jet main axis (i.e. the emitting region is decelerating while moving away from the core). However, observations indicate that a stratified geometry, with a fast spine surrounded by a slow layer in its simplest configuration, is equally possible. Interestingly, in a handful of sources, imaging in the radio to sub-mm band with very-long-baseline interferometry have probed AGN jets down to hundreds of gravitational radii from the central BH and revealed a limb-brightened transversal structure (see Mrk 501, M 87, Cygnus A and 3C 84; Giroletti et al. 2004; Nagai et al. 2014; Boccardi et al. 2016; Hada et al. 2016; Giovannini et al. 2018). These results suggest that mildly relativistic, emitting regions may be present already at sub-pc scales. Given the limited sample, it is not yet clear whether all jets, independently from their power, develop the same structure at small scales and how such a structure relates to the morphological differences that are seen at kiloparsec scales (FR I and FR II types, see for example the case of PKS 1127 − 145; Siemiginowska et al. 2007). Indeed, because of the long time-scales of the radio duty cycles in AGNs ($\gtrsim 10^7$ yr; Shabala et al. 2008; Brienza et al. 2017; and references therein), it is not easy to determine the factor(s) shaping the morphology of the giant RGs. The role of the environment where the radio source forms as well as the connection with the different accretion modes of the AGN are currently under investigation (see e.g. Ledlow & Owen 1996 ; Best 2009; Miraghaei & Best 2017; Croston, Ineson & Hardcastle 2018). Because of BH mass scaling relations, precious insights on the nature of the accretion and ejection phenomena come from X-ray binaries hosting stellar mass black holes, whose radio outbursts are typically observable on human time-scales (see Fender & Gallo 2014, for a review).

The acceleration mechanisms and radiative processes active in the jet's layer could be different from those in the highly relativistic spine. For example, continuous acceleration of ultrarelativistic electrons in turbulent boundary layers has been proposed to explain the X-ray synchrotron emission of FR I jets at kiloparsec scales (Stawarz & Ostrowski 2002, and references therein), whereas strong shocks and magnetic reconnection are candidate processes in

the spine (see e.g. Giannios 2013; Sironi, Petropoulou & Giannios 2015; Nalewajko 2016). In IC 1531, an SSC process can account for the observed emission and returns rather standard jet parameters and powers. However, in other MAGNs (e.g. 3C 84, NGC 6251; Tavecchio & Ghisellini 2014; Migliori et al. 2011), an SSC model implies extreme jet parameters (in terms of e.g. pressure, magnetization..), which would challenge the jet stability, or very large powers. On the other hand, the synchrotron emission produced by the spine(/layer) represents a natural source of seed photons for the electrons in the layer(/spine). Models of jets with multiple, radiatively interacting regions have been proved effective in reproducing the GeV and even TeV emission of some of the MAGN (Georganopoulos & Kazanas 2003; Ghisellini et al. 2005).

To conclude, although disfavoured by the observations, we briefly discuss the case of an aligned jet (say $\theta = 5^\circ$). Remarkably, this would make IC 1531 the BL Lac in the 3FGL with the lowest known redshift. Its radio luminosity ($L_r \sim 10^{39.9}$ erg s^{-1}) places IC 1531 in the lower radio-luminosity boundary of the class. This is a relatively unexplored regime because the identification of intrinsically faint BL Lac objects can be challenging (see Capetti & Raiteri 2015, for a discussion), and yet extremely important in order to build their luminosity function (LF). Using their developed selection method based on mid-infrared emission, Capetti & Raiteri (2015) argued in favour of a break in the local BL Lac LF at $L_r \sim 10^{40.6}$ erg s^{-1}, which could be possibly related to the power necessary to launch a jet. In the BL Lac scenario, IC 1531 would fall below this break. Detections of intrinsically faint γ-ray BL Lacs at low redshift are key to define the local γ-ray LF of this class and investigate a possible cosmological evolution, allowing also to estimate their contribution to the isotropic γ-ray background (Ajello et al. 2014).

9 SUMMARY AND CONCLUSIONS

In this paper, we performed a multiwavelength study of the radio source IC 1531, associated with the γ-ray source 3FGL J0009 − 3206. Its large-scale radio and X-ray morphologies and different diagnostic methods in the optical to infrared bands suggest that the source is likely an FR I RG whose jet is seen at moderate inclination angles ($\theta \sim 15^\circ$). As such, we propose IC 1531 as a member of the MAGNs detected by LAT. The γ-ray flux can be explained in terms of SSC emission from a region with $\Gamma_{\rm bulk} \sim 4$. In the framework of the unified scheme of AGNs, this supports the presence of multiple emitting regions with different velocities, such could be a spine-layer structure. Intriguingly, the processes that accelerate the particles radiating at high energies could be different with respect to those in the highly relativistic regions of blazars, possibly explaining some of the observational differences between blazars and MAGNs (such as e.g. the lack of significant variability and flares in X-to-γ-rays). High-energy and multiwavelength studies of a larger number of sources at the boundaries between RGs and blazars have the potential to provide us with a tomography of the jet regions where the most energetic emission is produced. The enhanced sensitivity reached by *Fermi* and the advent of large-field, sky-surveying observatories such as CTA, eROSITA, LSST, and SKA will be key to make progress in this research.

ACKNOWLEDGEMENTS

The research leading to these results has received funding from the European Unionś Horizon 2020 Programme under AHEAD project (grant agreement n. 654215). Partial support to this work was provided by the NASA grant AR4-15009X. GM acknowledges the financial support from the UnivEarthS Labex program of Sorbonne Paris Cité (ANR10LABX0023 and ANR11IDEX000502). We thank the anonymous referee for comments and suggestions that helped us to improve the manuscript. TB acknowledges financial contribution from the agreement ASI-INAF n.2017-14-H.0. MAPT acknowledges support from the Spanish MINECO through grants AYA2012-38491-C02-02 and AYA2015-63939- C2-1-P. AS was supported by NASA contract NAS8-03060 (*Chandra* X-ray Center). ET acknowledges financial support from ASI-INAF grant 2015- 023-R.O. We acknowledge financial support from PRIN INAF 2016. This work has used data supplied by the UK Swift Science Data Centre at the University of Leicester and archival data from the VLA. The NRAO a facility of the National Science Foundation operated under cooperative agreement by Associated Universities, Inc.

REFERENCES

Abdo A. A. et al., 2010a, Science, 328, 725
Abdo A. A. et al., 2010b, ApJ, 716, 30
Abdo A. A. et al., 2010c, ApJ, 720, 912
Ackermann M. et al., 2012, ApJ, 755, 164
Ackermann M. et al., 2015, ApJ, 810, 14
Ackermann M. et al., 2017, ApJ, 837, L5
Ajello M. et al., 2012, ApJ, 751, 108
Ajello M. et al., 2014, ApJ, 780, 73
Avni Y., 1976, ApJ, 210, 642
Baldi R. D., Capetti A., Giovannini G., 2015, A&A, 576, A38
Best P. N., 2009, Astron. Nachr., 330, 184
Best P. N., Heckman T. M., 2012, MNRAS, 421, 1569
Boccardi B., Krichbaum T. P., Bach U., Bremer M., Zensus J. A., 2016, A&A, 588, L9
Brienza M. et al., 2017, A&A, 606, A98
Buttiglione S., Capetti A., Celotti A., Axon D. J., Chiaberge M., Macchetto F. D., Sparks W. B., 2009, A&A, 495, 1033
Capetti A., Raiteri C. M., 2015, A&A, 580, A73
Capetti A., Massaro F., Baldi R. D., 2017a, A&A, 598, A49
Capetti A., Massaro F., Baldi R. D., 2017b, A&A, 601, A81
Casadio C. et al., 2015, ApJ, 808, 162
Cash W., 1979, ApJ, 228, 939
Celotti A., Ghisellini G., 2008, MNRAS, 385, 283
Chiaberge M., Celotti A., Capetti A., Ghisellini G., 2000, A&A, 358, 104
Condon J. J., Cotton W. D., Greisen E. W., Yin Q. F., Perley R. A., Taylor G. B., Broderick J. J., 1998, AJ, 115, 1693
Croston J. H., Ineson J., Hardcastle M. J., 2018, MNRAS, 476, 1614
D'Ammando F. et al., 2015, MNRAS, 450, 3975
D'Ammando F., Orienti M., Finke J., Larsson J., Giroletti M., Raiteri C., 2016, Galaxies, 4, 11
Di Mauro M., Calore F., Donato F., Ajello M., Latronico L., 2014, ApJ, 780, 161
Ekers R. D. et al., 1989, MNRAS, 236, 737
Evans P. A. et al., 2009, MNRAS, 397, 1177
Fender R., Gallo E., 2014, Space Sci. Rev., 183, 323
Fermi-LAT Collaboration, 2015, ApJS, 218, 23
Fornasa M., Sánchez-Conde M. A., 2015, Phys. Rep., 598, 1
Foschini L. et al., 2011, MNRAS, 413, 1671
Georganopoulos M., Kazanas D., 2003, ApJ, 594, L27
Ghisellini G., 2013a, Mem. Soc. Astron. Ital., 84, 719
Ghisellini G., 2013b, Lecture Notes in Physics, Vol. 873, Radiative Processes in High Energy Astrophysics. Springer International Publishing, Switzerland

Ghisellini G., Tavecchio F., Chiaberge M., 2005, A&A, 432, 401
Ghisellini G., Tavecchio F., Foschini L., Ghirlanda G., 2011, MNRAS, 414, 2674
Giannios D., 2013, MNRAS, 431, 355
Giovannini G., Cotton W. D., Feretti L., Lara L., Venturi T., 2001, ApJ, 552, 508
Giovannini G. et al., 2018, Nat. Astron., 2, 472
Giroletti M. et al., 2004, ApJ, 600, 127
Grandi P., Palumbo G. G. C., 2007, ApJ, 659, 235
Grandi P., Torresi E., Stanghellini C., 2012, ApJ, 751, L3
Grandi P., Capetti A., Baldi R. D., 2016, MNRAS, 457, 2
Hada K. et al., 2016, ApJ, 817, 131
Harris D. E., Krawczynski H., 2006, ARA&A, 44, 463
Heckman T. M., Kauffmann G., Brinchmann J., Charlot S., Tremonti C., White S. D. M., 2004, ApJ, 613, 109
Inoue Y., 2011, ApJ, 733, 66
Ishwara-Chandra C. H., Saikia D. J., 1999, MNRAS, 309, 100
Jones D. H. et al., 2004, MNRAS, 355, 747
Jones D. H. et al., 2009, MNRAS, 399, 683
Kalberla P. M. W., Burton W. B., Hartmann D., Arnal E. M., Bajaja E., Morras R., Pöppel W. G. L., 2005, A&A, 440, 775
Kataoka J. et al., 2011, ApJ, 740, 29
Kennicutt R. C., Jr, 1998, ARA&A, 36, 189
Knapp G. R., Patten B. M., 1991, AJ, 101, 1609
Knapp G. R., Bies W. E., van Gorkom J. H., 1990, AJ, 99, 476
Large M. I., Cram L. E., Burgess A. M., 1991, Observatory, 111, 72
Lavalley M., Isobe T., Feigelson E., 1992, in Worrall D. M., Biemesderfer C., Barnes J., eds, ASP Conf. Ser. Vol. 25, Astronomical Data Analysis Software and Systems I. Astron. Soc. Pac., San Francisco, p. 245
Ledlow M. J., Owen F. N., 1996, AJ, 112, 9
Loveday J., 1996, MNRAS, 278, 1025
Mahony E. K. et al., 2011, MNRAS, 417, 2651
Mannucci F., Basile F., Poggianti B. M., Cimatti A., Daddi E., Pozzetti L., Vanzi L., 2001, MNRAS, 326, 745
Maraschi L., Ghisellini G., Celotti A., 1992, ApJ, 397, L5
Marconi A., Hunt L. K., 2003, ApJ, 589, L21
Massaro F., Marchesini E. J., D'Abrusco R., Masetti N., Andruchow I., Smith H. A., 2017, ApJ, 834, 113
Mauch T., Murphy T., Buttery H. J., Curran J., Hunstead R. W., Piestrzynski B., Robertson J. G., Sadler E. M., 2003, MNRAS, 342, 1117
Migliori G. et al., 2011, A&A, 533, A72
Migliori G., Siemiginowska A., Kelly B. C., Stawarz L., Celotti A., Begelman M. C., 2014, ApJ, 780, 165
Migliori G., Siemiginowska A., Sobolewska M., Loh A., Corbel S., Ostorero L., Stawarz L., 2016, ApJ, 821, L31
Mirabel I. F., Rodríguez L. F., 1999, ARA&A, 37, 409
Miraghaei H., Best P. N., 2017, MNRAS, 466, 4346
Murphy T. et al., 2010, MNRAS, 402, 2403
Nagai H. et al., 2010, PASJ, 62, L11
Nagai H. et al., 2014, ApJ, 785, 53
Nalewajko K., 2016, Galaxies, 4, 28
O'Sullivan E., Sanderson A. J. R., Ponman T. J., 2007, MNRAS, 380, 1409
Padovani P. et al., 2017, A&AR, 25, 2
Planck Collaboration XIII, 2016, A&A, 594, A13
Sahakyan N., Baghmanyan V., Zargaryan D., 2018, A&A, 614, A6
Sambruna R. M., Donato D., Tavecchio F., Maraschi L., Cheung C. C., Urry C. M., 2007, ApJ, 670, 74
Shabala S. S., Ash S., Alexander P., Riley J. M., 2008, MNRAS, 388, 625
Shimmins A. J., Bolton J. G., 1974, Aust. J. Phys. Astrophys. Suppl., 32, 1
Siemiginowska A., Stawarz L., Cheung C. C., Harris D. E., Sikora M., Aldcroft T. L., Bechtold J., 2007, ApJ, 657, 145
Sikora M., Begelman M. C., Rees M. J., 1994, ApJ, 421, 153
Singal A. K., 1993, MNRAS, 263, 139
Sironi L., Petropoulou M., Giannios D., 2015, MNRAS, 450, 183
Skrutskie M. F. et al., 2006, AJ, 131, 1163
Slee O. B., Sadler E. M., Reynolds J. E., Ekers R. D., 1994, MNRAS, 269, 928
Stawarz L., Ostrowski M., 2002, ApJ, 578, 763
Stickel M., Padovani P., Urry C. M., Fried J. W., Kuehr H., 1991, ApJ, 374, 431
Sun X.-n., Yang R.-z., Mckinley B., Aharonian F., 2016, A&A, 595, A29
Tanada K., Kataoka J., Arimoto M., Akita M., Cheung C. C., Digel S. W., Fukazawa Y., 2018, ApJ, 860, 74
Tanaka Y. T., Doi A., Inoue Y. et al., 2015, ApJL, 799, L18
Tavecchio F., Ghisellini G., 2014, MNRAS, 443, 1224
Tavecchio F., Maraschi L., Ghisellini G., 1998, ApJ, 509, 608
Tavecchio F., Righi C., Capetti A., Grandi P., Ghisellini G., 2018, MNRAS, 475, 5529
Torresi E., Grandi P., Capetti A., Giovannini G., 2018, MNRAS, 476, 5535
Urry C. M., Padovani P., 1995, PASP, 107, 803
van Gorkom J. H., Knapp G. R., Ekers R. D., Ekers D. D., Laing R. A., Polk K. S., 1989, AJ, 97, 708
Volonteri M., Haardt F., Ghisellini G., Della Ceca R., 2011, MNRAS, 416, 216
Wright E. L. et al., 2010, AJ, 140, 1868

APPENDIX A: SOME EXTRA MATERIAL

In Table A1, we report the informations relative to the flux measurements in the radio to γ-ray band used to compile the SED of IC 1531.

Table A1. Multiwavelength data of IC 1531 taken from the literature and online data bases. Columns: (1) observed frequency; (2) flux and error (when available); (3) angular resolution of the instrument; and (4) references and mission data base.

Frequency (Hz)	Flux (erg cm^{-2} s^{-1})	Angular resolution	Reference
7.4×10^{7}	$(9.3 \pm 1.1) \times 10^{-16}$	80 arcsec	*VLSS*
4.08×10^{8}	$(3.1 \pm 0.2) \times 10^{-15}$	3 arcmin	Large, Cram & Burgess (1991)
8.43×10^{8}	$(3.8 \pm 0.1) \times 10^{-15}$	–	Mauch et al. (2003)
1.4×10^{9}	$(5.4 \pm 0.2) \times 10^{-15}$	45 arcsec	*NVSS*
1.47×10^{9}	3.4×10^{-15}	1 arcsec	van Gorkom et al. (1989)
2.3×10^{9}	3.0×10^{-15}	90mas	Slee et al. (1994)
2.7×10^{9}	$(13.0 \pm 0.5) \times 10^{-15}$	8 arcmin	Shimmins & Bolton (1974)
4.8×10^{9}	1.4×10^{-14}	5 arcsec	–
4.9×10^{9}	1.1×10^{-14}	VLA	–
5×10^{9}	$(15.7 \pm 0.8) \times 10^{-15}$	10.8 arcsec × 10.8 arcsec	Murphy et al. (2010)
5×10^{9}	$(17.5 \pm 1) \times 10^{-15}$	8 arcmin	–
8×10^{9}	$(2.2 \pm 0.1) \times 10^{-14}$	10.8 arcsec × 10.8 arcsec	–
8.4×10^{9}	2.4×10^{-14}	27mas	–
2×10^{10}	$(4.4 \pm 0.2) \times 10^{-14}$	10.8 arcsec × 10.8 arcsec	–
1.499×10^{11}	$(2.2 \pm 0.4) \times 10^{-13}$	27.5 arcsec	Knapp & Patten (1991)
2.306×10^{11}	$(2.9 \pm 0.6) \times 10^{-13}$	19.5 arcsec	–
2.725×10^{11}	$(2.4 \pm 0.4) \times 10^{-13}$	18.5 arcsec	–
2.998×10^{12}	$(1.4 \pm 0.5) \times 10^{-11}$	3.5 arcmin	Knapp et al. (1990)
3.747×10^{11}	$(9.9 \pm 1.6) \times 10^{-13}$	17 arcsec	–
1×10^{11}	$(2.6 \pm 0.5) \times 10^{-13}$	–	*PR2-2015 (Planck Legacy Archive)*
2.17×10^{11}	$(3.3 \pm 0.6) \times 10^{-13}$	–	–
1.363×10^{13}	$(17.9 \pm 0.2) \times 10^{-13}$	12.0 arcsec	*WISE*
2.498×10^{13}	$(18.2 \pm 0.5) \times 10^{-13}$	6.5 arcsec	–
6.517×10^{13}	$(7.8 \pm 0.2) \times 10^{-12}$	6.4 arcsec	–
8.817×10^{13}	$(18.6 \pm 0.4) \times 10^{-12}$	6.1 arcsec	–
1.388×10^{14}	$(12.2 \pm 0.4) \times 10^{-11}$	2 arcsec	*2MASS*
1.388×10^{14}	$(14.1 \pm 0.4) \times 10^{-11}$	2 arcsec	–
1.806×10^{14}	$(18.8 \pm 0.5) \times 10^{-11}$	2 arcsec	–
1.806×10^{14}	$(20.9 \pm 0.6) \times 10^{-11}$	2 arcsec	–
2.418×10^{14}	$(22.3 \pm 0.4) \times 10^{-11}$	2 arcsec	–
2.418×10^{14}	$(26.0 \pm 0.5) \times 10^{-11}$	2 arcsec	–
3.893×10^{14}	$(8.0 \pm 0.3) \times 10^{-11}$	–	*AAVSO*
4.797×10^{14}	$(6.9 \pm 0.2) \times 10^{-11}$	–	–
6.246×10^{14}	$(4.31 \pm 0.05) \times 10^{-11}$	–	–
1.292×10^{15}	$(2.6 \pm 0.2) \times 10^{-12}$	6 arcsec	*GALEX*
1.947×10^{15}	$(1.2 \pm 0.2) \times 10^{-12}$	4 arcsec	–
4.84×10^{22}	$<1.6 \times 10^{-12}$	–	Fermi2FglLC
4.84×10^{22}	$(9.0 \pm 4.9) \times 10^{-13}$	–	Fermi3FGL
1.452×10^{23}	$<1.9 \times 10^{-12}$	–	Fermi2FglLC
1.452×10^{23}	$(6.6 \pm 2.4) \times 10^{-13}$	–	Fermi3FGL
2.42×10^{23}	$(2.5 \pm 1.1) \times 10^{-12}$	–	Fermi2FglLC
4.84×10^{23}	$(1.3 \pm 0.4) \times 10^{-12}$	–	Fermi2FglLC
4.84×10^{23}	$(5.3 \pm 1.9) \times 10^{-13}$	–	Fermi3FGL
1.452×10^{24}	$<1.1 \times 10^{-12}$	–	Fermi2FglLC
1.452×10^{24}	$(2.7 \pm 1.7) \times 10^{-13}$	–	Fermi3FGL
1.452×10^{25}	$<1.3 \times 10^{-12}$	–	Fermi2FglLC
1.452×10^{25}	$(1.2 \pm 0.9) \times 10^{-13}$	–	Fermi3FGL

APPENDIX B: CONSTRAINTS

In this section, we detail the procedure that we followed to derive constraints on the jet's inclination angle and speed.

The flux density ratio of the approaching to the receding component, S_a and S_r, can be written as follows (Mirabel & Rodríguez 1999):

$$R \equiv \frac{S_a}{S_r} = \left(\frac{1 + \beta \cos\ \theta}{1 - \beta \cos\ \theta} \right)^{k-\alpha},$$

where $\frac{S_a}{S_o} = \delta_a^{k-\alpha}$, $\frac{S_r}{S_o} = \delta_r^{k-\alpha}$, are the ratios of observed to emitted flux densities of the approaching and receding components, $\beta = v/c$

is the intrinsic jet speed, in units of c, θ is the angle of the jet to the line of sight, α is the spectral index of the emission ($S_\nu \propto \nu^\alpha$), and k is a parameter that accounts for the geometry of the ejecta, with $k = 2$ for a continuous jet and $k = 3$ for discrete condensations.

The (true) jet speed β and the bulk Lorentz factor, $\Gamma_{\rm bulk}$, are related as follows: $\Gamma_{\rm bulk} = (1 - \beta^2)^{-1/2}$, so that $\beta = (1 - \Gamma^{-2})^{1/2}$. Although we lack a precise knowledge of the values of β and/or θ, we know that for the angle θ_m that maximizes the value of β the following equality applies: $\cos\theta_m = \beta$. Hence,

$$\cos\ \theta_m = \beta = (1 - \Gamma_{\rm bulk}^{-2})^{1/2},$$

and we get

$$\frac{1 + \beta\cos\ \theta_m}{1 - \beta\cos\ \theta_m} = \frac{1 + \beta^2}{1 - \beta^2} = \frac{1 + (1 - \Gamma_{\rm bulk}^{-2})}{\Gamma_{\rm bulk}^{-2}} = 2\,\Gamma_{\rm bulk}^2 - 1.$$

Substituting in the Equation for R and rearranging, we get the angle θ_m that maximizes β (and therefore $\Gamma_{\rm bulk}$), as a function of the flux density ratio, R:

$$\theta_m = \arccos\left(\frac{R^m - 1}{R^m + 1}\right)^{1/2},$$

where $m = 1/(k - \alpha)$. We assume $k = 2, 3$, no significant variability between the L-band and X-band observations, and flux uncertainties within 10 per cent. For the nominal flux values, we obtain $\theta_m = 14.8^\circ$, $\beta = 0.967$, and $\Gamma_{\rm bulk} = 3.93$, with a range of values for the angle θ_m spanning between 10° and 20°.

This paper has been typeset from a TEX/LATEX file prepared by the author.